

## Tuning the Charge-Transport Parameters of Perylene Diimide Single Crystals via End and/or Core Functionalization: A Density Functional Theory Investigation

M. Carmen Ruiz Delgado, Eung-Gun Kim, Demétrio A. da Silva Filho, and Jean-Luc Bredas\*

*School of Chemistry and Biochemistry & Center for Organic Photonics and Electronics, Georgia Institute of Technology, Atlanta, Georgia 30332-0400*

Received September 25, 2009; E-mail: jean-luc.bredas@chemistry.gatech.edu

**Abstract:** Perylene tetracarboxylic diimide (PTCDI) derivatives stand out as one of the most investigated families of air-stable *n*-type organic semiconductors for organic thin-film transistors. Here, we use density functional theory to illustrate how it is possible to control the charge-transport parameters of PTCDIs as a function of the type, number, and positions of the substituents. Specifically, two strategies of functionalization related to core and end substitutions are investigated. While end-substituted PTCDIs present the same functional molecular backbone, their molecular packing in the crystal significantly varies; as a consequence, this series of derivatives constitutes an ideal test bed to evaluate the models that describe charge-transport in organic semiconductors. Our results indicate that large bandwidths along with small effective masses can be obtained with the insertion of appropriate substituents on the nitrogens, in particular halogenated aromatic groups.

### 1. Introduction

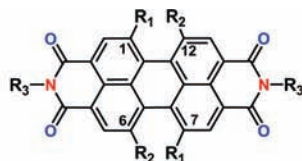
Perylene tetracarboxylic diimides (PTCDIs) (see Figure 1) are among the most promising and versatile candidates for organic (opto)electronic applications due to their commercial availability, low cost, and electronic, optical, and charge-transport properties that can be tuned over a wide range via judicious functionalization.<sup>1–3</sup> Importantly, PTCDIs form an appealing class of *n*-channel semiconductors for organic field-effect transistors (OFETs) because of their high electron affinity and large electron mobility in the solid state.<sup>4–11</sup> They are also exploited as the electron-acceptor component in organic solar cells.<sup>12–17</sup>

PTCDIs typically arrange in  $\pi$ -stacks, in which the extent of intermolecular  $\pi$ -orbital overlap varies greatly among the derivatives. Two strategies of functionalization have been exploited for the design of air-stable *n*-channel PTCDIs: (i) end functionalization or substitution on the imide nitrogens<sup>1,6,10,11,18,19</sup> and (ii) core functionalization, or substitution in positions 1, 6,

7, and/or 12 (see Figure 1).<sup>3–5,7–9,20,21</sup> While the former maintains the planarity of the perylene aromatic core, the latter leads to a varying degree of distortion in the core due to the steric hindrance present in the bay region. Interestingly, in spite of their distorted perylene skeletons, substantial electron mobilities have been demonstrated when introducing strongly electron withdrawing groups onto the perylene core.<sup>5,7,9,22</sup>

- (1) Chesterfield, R. J.; McKeen, J. C.; Newman, C. R.; Ewbank, P. C.; da Silva, D. A.; Bredas, J. L.; Miller, L. L.; Mann, K. R.; Frisbie, C. D. *J. Phys. Chem. B* **2004**, *108*, 19281–19292.
- (2) Wurthner, F. *Chem. Commun.* **2004**, 1564–1579.
- (3) Jones, B. A.; Facchetti, A.; Wasielewski, M. R.; Marks, T. J. *J. Am. Chem. Soc.* **2007**, *129*, 15259–15278.
- (4) Chen, Z. J.; Debije, M. G.; Debaerdemaeker, T.; Osswald, P.; Wurthner, F. *ChemPhysChem* **2004**, *5*, 137–140.
- (5) Jones, B. A.; Ahrens, M. J.; Yoon, M. H.; Facchetti, A.; Marks, T. J.; Wasielewski, M. R. *Angew. Chem., Int. Ed.* **2004**, *43*, 6363–6366.
- (6) Chen, H. Z.; Ling, M. M.; Mo, X.; Shi, M. M.; Wang, M.; Bao, Z. *Chem. Mater.* **2007**, *19*, 816–824.
- (7) Schmidt, R.; Ling, M. M.; Oh, J. H.; Winkler, M.; Konemann, M.; Bao, Z. N.; Wurthner, F. *Adv. Mater.* **2007**, *19*, 3692–3695.
- (8) Weitz, R. T.; Amsharov, K.; Zschieschang, U.; Villas, E. B.; Goswami, D. K.; Burghard, M.; Dosch, H.; Jansen, M.; Kern, K.; Klauk, H. *J. Am. Chem. Soc.* **2008**, *130*, 4637–4645.

- (9) Molinari, A. S.; Alves, H.; Chen, Z.; Facchetti, A.; Morpurgo, A. F. *J. Am. Chem. Soc.* **2009**, *131*, 2462–2463.
- (10) Oh, J. H.; Lee, H. W.; Mannsfeld, S.; Stoltenberg, R. M.; Jung, E.; Jin, Y. W.; Kim, J. M.; Yoo, J. B.; Bao, Z. N. *Proc. Natl. Acad. Sci. U.S.A.* **2009**, *106*, 6065–6070.
- (11) Wen, Y. G.; Liu, Y. Q.; Di, C. A.; Wang, Y.; Sun, X. N.; Guo, Y. L.; Zheng, J.; Wu, W. P.; Ye, S. H.; Yu, G. *Adv. Mater.* **2009**, *21*, 1631–1635.
- (12) Tang, C. W. *Appl. Phys. Lett.* **1986**, *48*, 183–185.
- (13) Wohrle, D.; Kreienhoop, L.; Schnurpfeil, G.; Elbe, J.; Tennigkeit, B.; Hiller, S.; Schlettwein, D. *J. Mater. Chem.* **1995**, *5*, 1819–1829.
- (14) Schmidt-Mende, L.; Fechtenkotter, A.; Mullen, K.; Moons, E.; Friend, R. H.; MacKenzie, J. D. *Science* **2001**, *293*, 1119–1122.
- (15) Shin, W. S.; Jeong, H. H.; Kim, M. K.; Jin, S. H.; Kim, M. R.; Lee, J. K.; Lee, J. W.; Gal, Y. S. *J. Mater. Chem.* **2006**, *16*, 384–390.
- (16) Wurthner, F.; Chen, Z. J.; Hoeben, F. J. M.; Osswald, P.; You, C. C.; Jonkheijm, P.; von Herrikhuyzen, J.; Schenning, A. P. H. J.; van der Schoot, P. P. A. M.; Meijer, E. W.; Beckers, E. H. A.; Meskers, S. C. J.; Janssen, R. A. J. *J. Am. Chem. Soc.* **2004**, *126*, 10611–10618.
- (17) Zhan, X. W.; Tan, Z. A.; Domercq, B.; An, Z. S.; Zhang, X.; Barlow, S.; Li, Y. F.; Zhu, D. B.; Kippelen, B.; Marder, S. R. *J. Am. Chem. Soc.* **2007**, *129*, 7246–7247.
- (18) Hosoi, Y.; Tsunami, D.; Hisao, I.; Furukawa, Y. *Chem. Phys. Lett.* **2007**, *436*, 139–143.
- (19) Oh, J. H.; Liu, S.; Bao, Z.; Schmidt, R.; Wurthner, F. *Appl. Phys. Lett.* **2007**, *91*, 212107.
- (20) Jones, B. A.; Facchetti, A.; Wasielewski, M. R.; Marks, T. J. *Adv. Funct. Mater.* **2008**, *18*, 1329–1339.
- (21) Li, Y.; Tan, L.; Wang, Z. H.; Qian, H. L.; Shi, Y. B.; Hu, W. P. *Org. Lett.* **2008**, *10*, 529–532.

(a) End-substituted PTCDIs:  $R_1 = R_2 = H$ 

$R_3$		$R_3$		$R_3$	
H	<b>1</b>	$H_2C-CH_2-CH_2-O-CH_3$	<b>11</b>	$H_2C-H_2C-$	<b>21</b>
CH <sub>3</sub>	<b>2</b>	$H_2C-CH_2-CH_2-O-CH_2-CH_3$	<b>12</b>	$H_2C-CH(CH_3)-$	<b>22</b>
CH <sub>2</sub> -CH <sub>3</sub>	<b>3</b>	$H_3C-C_6H_4-$	<b>13</b>	$H_2C-H_2C-H_2C-$	<b>23</b>
$H_2C-CH_2-CH_3$	<b>4</b>	$H_3C-C_6H_4-O-CH_2-CH_3$	<b>14</b>	$H_2C-C_6H_4-OCH_3$	<b>24</b>
$H_2C-CH_2-CH_2-CH_3$	<b>5</b>	$H_3C-C_6H_4-N=N-C_6H_5$	<b>15</b>	$H_2C-C_6H_3(F)-Cl$	<b>25</b>
$H_2C-CH_2-CH_2-CH_2-CH_3$	<b>6</b>	$C_5H_4N-$	<b>16</b>	$H_2C-C_6H_3(F)_2-Cl$	<b>26</b>
$H_3C-CH(CH_3)-CH_2-CH_3$	<b>7</b>	$C_5H_3N-$	<b>17</b>	$H_2C-C_6H_3(F)_2-Cl$	<b>27</b>
$H_2C-CH_2-CH_2-CH_2-CH_2-CH_2-CH_3$	<b>8</b>	$C_5H_4N-$	<b>18</b>	$H_2C-C_6H_3(F)-Cl$	<b>28</b>
$H_2C-CH_2-CH_2-CH_2-OH$	<b>9</b>	$H_2C-C_6H_4-$	<b>19</b>	$H_2C-C_6H_3(F)_2-Cl$	<b>29</b>
$H_2C-CH_2-CH_2-O-CH_2-CH_3$	<b>10</b>	$H_2C-H_2C-C_6H_4-$	<b>20</b>	$H_2C-C_6H_3(F)_2-Cl$	<b>30</b>

(b) Core- and core/end-substituted PTCDIs

$R_1$	$R_2$	$R_3$		$R_1$	$R_2$	$R_3$	
Br	H	H	1,7-dibromo <b>PTCDI-Br<sub>2</sub></b>	F	H	H	1,7-difluoro <b>PTCDI-F<sub>2</sub></b>
CN	H	H	1,7-dicyano <b>PTCDI-CN<sub>2</sub></b>	F	F	H	1,6,7,12-tetrafluoro <b>PTCDI-F<sub>4</sub></b>
Cl	Cl	H	1,6,7,12-tetrachloro <b>PTCDI-Cl<sub>4</sub></b>	F	H	$H_2C-C(F)_2-CF_3$	1,7-difluoro <b>PBIF<sub>2</sub></b>
				F	F	$H_2C-C(F)_2-CF_3$	1,6,7,12-tetrafluoro <b>PBIF<sub>4</sub></b>

**Figure 1.** Chemical structures of (a) the end-substituted and (b) the core- and core/end-substituted PTCDIs examined in this study with the labeling used throughout this work.

We recall that PTCDIs are well-known organic pigments<sup>23</sup> that cover a variety of colors in the solid state from red to maroon to black. One of the most important features of these materials in their application as commercial paint pigments is their crystallochromy (i.e., the dependence of color on crystal packing). This property was investigated in depth, both experimentally and theoretically, for a large number of end-functionalized PTCDI single crystals; it was demonstrated that the intermolecular packing greatly impacts the optical properties. Klebe et al. developed an empirical model to rationalize the visible absorption maxima as a function of the  $\pi$ - $\pi$  contact area between stacked PTCDI molecules.<sup>24</sup> Kazmaier and Hoff-

mann found a strong correlation between crystal color and both longitudinal and transverse intermolecular offsets, based on tight-binding extended Hückel calculations.<sup>25</sup> More recently, Zhao et al. have been able to reproduce the excitation energies of the PTCDI crystal structures by using a theoretical protocol based on time-dependent Hartree-Fock (TD-HF) calculations on dimers;<sup>26</sup> their results provide good evidence that the electronically excited states, which determine the color of these pigments, have no significant charge-transfer character.

(22) Ling, M. M.; Erk, P.; Gomez, M.; Koenemann, M.; Locklin, J.; Bao, Z. N. *Adv. Mater.* **2007**, *19*, 1123–1127.

(23) Herbst, W.; Hunger, K. *Industrial Organic Pigments: Production, Properties, Applications*, 2nd ed.; Wiley-VCH: Weinheim, Germany, 1997.

(24) Klebe, G.; Graser, F.; Hadicke, E.; Berndt, J. *Acta Crystallogr., Sect. B: Struct. Sci.* **1989**, *45*, 69–77.

(25) Kazmaier, P. M.; Hoffmann, R. *J. Am. Chem. Soc.* **1994**, *116*, 9684–9691.

(26) Zhao, H. M.; Pfister, J.; Settels, V.; Renz, M.; Kaupp, M.; Dehm, V. C.; Wurthner, F.; Fink, R. F.; Engels, B. *J. Am. Chem. Soc.* **2009**, *131*, 15660–15668.

In the present work, we investigate at the density functional theory (DFT) level over 30 existing PTCDis, only a handful of which have been exploited experimentally for their charge-transport properties. We analyze how the variations in solid-state packing as a function of the nature and positions of the substituents affect the charge-transport parameters. First, we focus on the frontier electronic states and electron–vibration coupling at the single-molecule level. We then evaluate the properties of the crystal structures using band structure and transfer integral calculations. The results provide a compelling illustration of the impact of intermolecular packing on the charge-transport parameters of semiconducting organic crystals and suggest new design strategies for the development of high-performance PTCDI-based electronic materials.

## 2. Theoretical Methodology

The molecular geometries of the neutral and radical ion states were optimized at the DFT level using the B3LYP functional<sup>27,28</sup> and the 6-31G\*\* basis set,<sup>29,30</sup> as implemented in the Gaussian 03 program.<sup>31</sup> On the basis of the resulting ground-state geometries, harmonic vibrational frequencies were calculated analytically at the same theoretical level. Single-point calculations were also performed using a more flexible basis set augmented with diffuse functions (6-31++G\*\*).<sup>32</sup> It was recently shown<sup>33</sup> that the DFT estimates of the reorganization energy depend on the amount of “exact” Hartree–Fock exchange included in the hybrid functional. Among the standard functionals considered, B3LYP provides the best description of the relaxation processes in oligoacenes,<sup>33</sup> as a result, we have chosen the B3LYP functional for the calculations of the electronic properties at the molecular level. The reorganization energies, ionization energies, and electron affinities were calculated directly from the relevant points on the potential energy surfaces using the standard procedure detailed in the literature.<sup>34</sup> The intramolecular reorganization energies were also evaluated with the DUSHIN code<sup>35</sup> using the results of the frequency calculations.

Calculations of the electronic band structures and densities of states of the end-substituted PTCDI crystals **1–30** and the core-/end-substituted **PBIF<sub>2</sub>** and **PBIF<sub>4</sub>** crystals of Figure 1 were performed without geometry optimization with the CRYSTAL06 program<sup>36</sup> using B3LYP. Given the large number of systems under study and the considerable size of the unit cells, the 6-31G basis set was used as a good compromise between accuracy and computational cost. In these calculations, a uniform Monkhorst–Pack *k*-point mesh<sup>37</sup> was employed (see the Supporting Information for more details). The lattice parameters and the atomic positions were

taken from the experimental crystal structures,<sup>7,24,38–47</sup> crystallographic parameters for the unit cells of all the PTCDI crystals are collected in Table S1 in the Supporting Information. Crystallographic data were retrieved from the Cambridge Structural Database.

For **26** and **PBIF<sub>2</sub>**, the inverse effective mass tensor was calculated from the band structure using Sperling’s centered difference method with  $dk = 0.0032$  ( $2\pi/\text{Å}$ ).<sup>48</sup> The optimization of the crystal electronic structure, followed by non-self-consistent calculations to compute the carrier effective masses, was performed with the PBE exchange–correlation functional. Vanderbilt ultrasoft pseudopotentials<sup>49</sup> were used with an energy cutoff of 25 Ry for the wave function (200 Ry for the electron density). Calculations were performed with the PWscf (plane-wave self-consistent field) code.<sup>50</sup> It has been recently shown<sup>51</sup> that band-structure calculations performed with the PBE exchange–correlation functional and a plane-wave basis set provide estimates of the bandwidths and band dispersions in very good agreement with those calculated at the B3LYP/6-31G level.

Finally, the transfer integrals for nearest-neighbor molecular pairs in the PTCDI crystals were calculated by using a fragment orbital approach<sup>52</sup> in combination with a basis set orthogonalization procedure.<sup>53</sup> We also computed the transfer integrals for model cofacial dimers of unsubstituted PTCDI when one of the molecules is translated along its long or short axis. These calculations were performed with the PW91 functional and Slater-type triple- $\zeta$  plus polarization (TZP) basis sets, using the ADF (Amsterdam density functional) package.<sup>54</sup> The PW91 functional was found by Huang and Kertesz to provide results in closest agreement with experimental values.<sup>55</sup> Regarding the choice of the basis set for the transfer integral calculations, it was shown for the pentacene<sup>53</sup> and ethylene<sup>56</sup> dimers that the TZP basis yields reliable results vs larger basis sets.

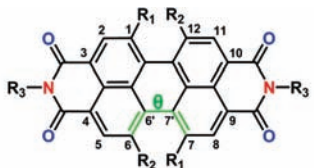
## 3. Results and Discussion

PTCDI derivatives **1–30**, which represent all end-functionalized PTCDI crystals found in the Cambridge Structural

- (27) Lee, C. T.; Yang, W. T.; Parr, R. G. *Phys. Rev. B* **1988**, *37*, 785–789.  
 (28) Becke, A. D. *J. Chem. Phys.* **1993**, *98*, 5648–5652.  
 (29) Hehre, W. J.; Ditchfield, R.; Pople, J. A. *J. Chem. Phys.* **1972**, *56*, 2257.  
 (30) Francl, M. M.; Pietro, W. J.; Hehre, W. J.; Binkley, J. S.; Gordon, M. S.; Defrees, D. J.; Pople, J. A. *J. Chem. Phys.* **1982**, *77*, 3654–3665.  
 (31) Frisch, M. J., et al. Gaussian 03, revision B.02; Gaussian, Inc., Pittsburgh, PA, 2003.  
 (32) Clark, T.; Chandrasekhar, J.; Spitznagel, G. W.; Schleyer, P. v. R. *J. Comput. Chem.* **1983**, *4*, 294–301.  
 (33) Sanchez-Carrera, R. S.; Coropceanu, V.; da Silva, D. A.; Friedlein, R.; Osikowicz, W.; Murdey, R.; Suess, C.; Salaneck, W. R.; Bredas, J. L. *J. Phys. Chem. B* **2006**, *110*, 18904–18911.  
 (34) (a) Bredas, J. L.; Beljonne, D.; Coropceanu, V.; Cornil, J. *Chem. Rev.* **2004**, *104*, 4971–5003. (b) Coropceanu, V.; Cornil, J.; da Silva Filho, D. A.; Olivier, Y.; Silbey, R.; Bredas, J. L. *Chem. Rev.* **2007**, *107*, 926–952.  
 (35) Reimers, J. R. *J. Chem. Phys.* **2001**, *115*, 9103–9109.  
 (36) Dovesi, R.; Saunders, V. R.; Roetti, C.; Orlando, R.; Zicovich-Wilson, C. M.; Pascale, F.; Civalieri, B.; Doll, K.; Harrison, N. M.; Bush, I. J.; D’Arco, P.; Llunell, M. *CRYSTAL06 User’s Manual*; University of Torino: Torino, Italy, 2006.  
 (37) Monkhorst, H. J.; Pack, J. D. *Phys. Rev. B* **1976**, *13*, 5188–5192.

- (38) Hadicke, E.; Graser, F. *Acta Crystallogr., Sect. C: Cryst. Struct. Commun.* **1986**, *42*, 189–195.  
 (39) Hadicke, E.; Graser, F. *Acta Crystallogr., Sect. C: Cryst. Struct. Commun.* **1986**, *42*, 195–198.  
 (40) Zugenmaier, P.; Duff, J.; Bluhm, T. L. *Cryst. Res. Technol.* **2000**, *35*, 1095–1115.  
 (41) Mizuguchi, J.; Tojo, K. *Z. Kristallogr.-New Cryst. Struct.* **2002**, *217*, 247–248.  
 (42) Tojo, K.; Mizuguchi, J. *Z. Kristallogr.-New Cryst. Struct.* **2002**, *217*, 517–518.  
 (43) Tojo, K.; Mizuguchi, J. *Z. Kristallogr.-New Cryst. Struct.* **2002**, *217*, 45–46.  
 (44) Mizuguchi, J.; Hino, K.; Sato, K.; Takahashi, H.; Suzuki, S. *Acta Crystallogr., Sect. E: Struct. Rep. Online* **2005**, *61*, O434–O436.  
 (45) Mizuguchi, J.; Hino, K.; Sato, K.; Takahashi, H.; Suzuki, S. *Acta Crystallogr., Sect. E: Struct. Rep. Online* **2005**, *61*, O437–O439.  
 (46) Hino, K.; Sato, K.; Takahashi, H.; Suzuki, S.; Mizuguchi, J. *Acta Crystallogr., Sect. E: Struct. Rep. Online* **2005**, *61*, O440–O441.  
 (47) Briseno, A. L.; Mannsfeld, S. C. B.; Reese, C.; Hancock, J. M.; Xiong, Y.; Jenekhe, S. A.; Bao, Z.; Xia, Y. *Nano Lett.* **2007**, *7*, 2847–2853.  
 (48) Kim, E. G.; Bredas, J. L. *J. Am. Chem. Soc.* **2008**, *130*, 16880–16889.  
 (49) Vanderbilt, D. *Phys. Rev. B* **1990**, *41*, 7892–7895.  
 (50) PWscf, 4.0.4; Democritos National Simulation Center of INFN, 2008.  
 (51) Delgado, M. C. R.; Pigg, K. R.; Filho, D. A. D. S.; Gruhn, N. E.; Sakamoto, Y.; Suzuki, T.; Osuna, R. M.; Casado, J.; Hernandez, V.; Navarrete, J. T. L.; Martinelli, N. G.; Cornil, J.; Sanchez-Carrera, R. S.; Coropceanu, V.; Bredas, J. L. *J. Am. Chem. Soc.* **2009**, *131*, 1502–1512.  
 (52) Senthikumar, K.; Grozema, F. C.; Bickelhaupt, F. M.; Siebbeles, L. D. A. *J. Chem. Phys.* **2003**, *119*, 9809–9817.  
 (53) Valeev, E. F.; Coropceanu, V.; da Silva, D. A.; Salman, S.; Bredas, J. L. *J. Am. Chem. Soc.* **2006**, *128*, 9882–9886.  
 (54) ADF, 2006.01; Scientific Computing and Modelling NV, Amsterdam, 2006.  
 (55) Huang, J. S.; Kertesz, M. *J. Chem. Phys.* **2005**, *122*, 234701.  
 (56) Huang, J. S.; Kertesz, M. *Chem. Phys. Lett.* **2004**, *390*, 110–115.

**Table 1.** Experimental and Calculated Torsion Angles  $\theta$  (Defined by  $C_6-C_6-C_7-C_7$ ) for the Core- and Core-/End-Substituted PTCDI Molecules

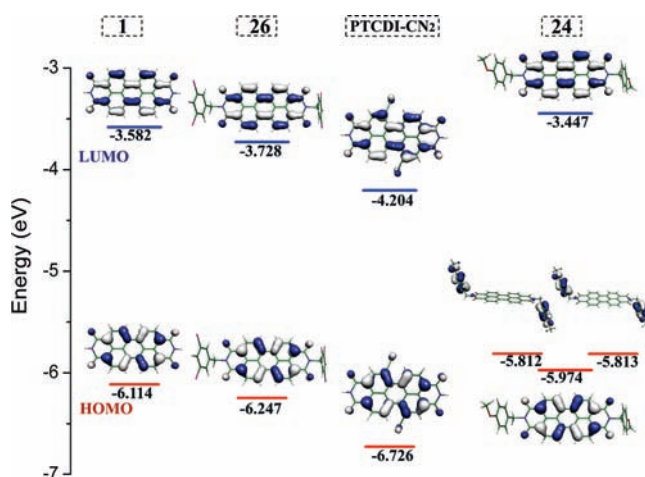


Compound	$\theta$ [ $^\circ$ ] <sup>a</sup>	$\theta$ [ $^\circ$ ] <sup>b</sup>
PTCDI-Br <sub>2</sub>	24 <sup>[Ref. 57]</sup>	23
PTCDI-CN <sub>2</sub>	5 <sup>[Ref. 5]</sup>	16 <sup>c</sup>
PTCDI-Cl <sub>4</sub>	37 <sup>[Ref. 4]</sup>	36
PBIF <sub>2</sub>	3 <sup>[Ref. 7]</sup>	5
PBIF <sub>4</sub>	25/19 <sup>d</sup> <sup>[Ref. 7]</sup>	25

<sup>a</sup> Determined by single-crystal X-ray analysis. For **PTCDI-Br<sub>2</sub>**, **PTCDI-CN<sub>2</sub>**, and **PTCDI-Cl<sub>4</sub>**, the structural data were taken from molecules with the same PTCDI core and different end substituents ( $R_3$  group) as well. <sup>b</sup> Calculated (B3LYP/6-31G\*\*) on isolated single molecules. <sup>c</sup> See ref 58 for the torsion angle values obtained with different theoretical methods. <sup>d</sup> Torsion angles of the perylene core at two bay areas.

Database, display flat perylene cores. The substituents on the imide nitrogen atoms consist of linear or branched alkyl (**1–8**),<sup>38,39,43,47</sup> alkyl alcohol (**9**),<sup>24</sup> alkyl ether (**10–12**),<sup>38</sup> aromatic (**13–18**),<sup>24,39,44–46</sup> and alkyl aromatic groups (**19–30**).<sup>38,40–42</sup> In the case of core and core-/end-substituted PTCDis, experimental crystal structures<sup>3–5,7,57</sup> reveal a distortion of the perylene core, which is mainly attributed to the steric hindrance of the substituents in the 1-, 6-, 7-, and/or 12-positions. The torsion angle  $\theta$  at the bay varies from 3 to 37° with different (numbers of) substituents, in the following order: **PBIF<sub>2</sub>** < **PTCDI-CN<sub>2</sub>** < **PTCDI-Br<sub>2</sub>** < **PBIF<sub>4</sub>** < **PTCDI-Cl<sub>4</sub>** (see Table 1). We note that the DFT torsion angles are in good agreement with the experimental data, except for **PTCDI-CN<sub>2</sub>**; this discrepancy can be attributed to the presence of specific packing effects, since calculations on isolated molecules obviously do not account for crystal-packing forces.<sup>58</sup>

**3.1. Single-Molecule “Transport” Levels.** Figure 2 compares the frontier molecular orbitals (MOs) of the unsubstituted PTCDI **1** with those of representative end- and/or core-substituted PTCDI molecules. Both the HOMO (highest occupied MO) and LUMO (lowest unoccupied MO) levels are of  $\pi$  nature and spread over the whole PTCDI core (with the exception of **24**; see discussion in section 3.3). It is interesting to note that both HOMO and LUMO orbitals present nodes along the long molecular axis and, thus, on the imide nitrogens; hence, end substituents are not expected to induce any significant alteration of the electronic properties of the individual PTCDI molecules. However, substitution directly on the perylene core is expected a priori to have a greater effect on the HOMO and LUMO energies, since the corresponding wave functions have contributions from the core substituents (see Figure 2).



**Figure 2.** Illustration of the frontier molecular orbitals for unsubstituted (**1**), end-substituted (**24**, **26**), and core-substituted (**PTCDI-CN<sub>2</sub>**) PTCDis.

Ionization potentials (IPs) and electron affinities (EAs) obtained from self-consistent-field ( $\Delta$ SCF) calculations are reported in Table 2 for a number of derivatives (see Table S2 in the Supporting Information for the results on all the PTCDI systems). It is seen that the trends in the vertical ionization energies are well captured by the one-electron molecular orbital picture; that is, Koopmans’ theorem (KT) applies well.<sup>59</sup> As expected, the HOMO and LUMO energies vary with the nature of the substituents; for instance, the strong electron-withdrawing effect of the cyano group stabilizes both the HOMO and the LUMO in a similar way (by  $\sim 0.6$  eV) in **PTCDI-CN<sub>2</sub>**, while the substitution of electron-donating alkyl ether groups on the imide nitrogens in **10–12** results in a destabilization (up to 0.2 eV) of the frontier molecular orbitals. In agreement with experimental data,<sup>60</sup> the chlorinated molecules are found to have a lower LUMO level than their fluorinated counterparts ( $-4.14$  eV for **PTCDI-F<sub>4</sub>** vs.  $-4.22$  eV for **PTCDI-Cl<sub>4</sub>**). Similar trends in EA and IP evolutions upon end and/or core substitutions are obtained when using an augmented basis set with diffuse functions (see Table 2 and Table S2). Better agreement with the experimental LUMO energies obtained from cyclic voltammetry (i.e.  $-3.9$  eV for **8**,<sup>3</sup>  $-4.1$  eV for **20**,<sup>3</sup>  $-4.2$  eV for dibromo core-substituted PTCDI,<sup>3</sup> and  $-4.3$  eV for dicyano core-substituted PTCDI<sup>3</sup>) is found at the B3LYP/6-31++G\*\*//B3LYP/6-31G\*\* level; this parallels recent results on oligoacenes.<sup>61</sup>

Interestingly, core substitution does not provide a stronger impact than end substitution; for instance, when two end substituents are compared to two core substituents, and not four, similar changes in the HOMO/LUMO energies ( $<0.25$  eV) are found (see Table 2). On the other hand, the effects of core and end substitutions are nearly additive (for example, the IP of **PBIF<sub>4</sub>** can be calculated from **PTCDI-F<sub>2</sub>** and **PBIF<sub>2</sub>** by adding the contributions from  $F_2$  and  $(CH_2C_3F_7)_2$ ). We note that the HOMO–LUMO gap is slightly more affected by the core functionalization because the direct, albeit weak, interactions with the perylene core are not the same in the two frontier MO levels (see Figure S1 in the Supporting Information).

(57) Wurthner, F.; Stepanenko, V.; Chen, Z. J.; Saha-Moller, C. R.; Kocher, N.; Stalke, D. *J. Org. Chem.* **2004**, *69*, 7933–7939.


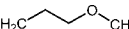
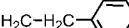
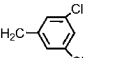
(58) Similar or even larger distortions of the perylene core are obtained when using various other computational methods: semiempirical PM3 (24°), HF/6-31G\*\* (19°), MP2/6-31G\*\* (18°), B3LYP/6-31++G\*\* (17°). Similar torsional angles have been previously observed in the 9-cyanodibenz[*a,c*]anthracene crystal: Duan, S.; Turk, J.; Speigle, J.; Corbin, J.; Masnovi, J.; Baker, R. J. *J. Org. Chem.* **2000**, *65*, 3005. A single crystal structure based on a dicyano core-substituted PTCDI is available in the literature, which severely restricts the correlation with the theoretical data.

(59) Koopmans, T. *Physica* **1934**, *1*, 104–113.

(60) Tang, M. L.; Oh, J. H.; Reichardt, A. D.; Bao, Z. N. *J. Am. Chem. Soc.* **2009**, *131*, 3733–3740.

(61) Winkler, M.; Houk, K. N. *J. Am. Chem. Soc.* **2007**, *129*, 1805–1815.

**Table 2.** Ionization Potentials and Electron Affinities of Various PTCDis Obtained from  $\Delta$ SCF and KT Calculations (Energies in eV)<sup>a</sup>

Compound	R <sub>3</sub> -Group	IP		EA <sup>b</sup>	
		Vertical	Koopmans <sup>c</sup>	Vertical	Koopmans <sup>c</sup>
<b>1</b>	<b>H</b>	7.43 (7.72)	6.11 (6.45)	-2.28 (-2.72)	-3.58 (-3.96)
<b>6</b>		7.23 (7.47)	5.97 (6.25)	-2.20 (-2.58)	-3.44 (-3.77)
<b>11</b>		7.19 (7.43)	5.93 (6.21)	-2.15 (-2.53)	-3.40 (-3.73)
<b>20</b>		7.17 (7.43)	6.03 (6.32)	-2.27 (-2.66)	-3.50 (-3.84)
<b>26</b>		7.40 (7.63)	6.25 (6.51)	2.52 (-2.87)	-3.73 (-4.04)
<b>PTCDI-Br<sub>2</sub></b>	<b>H</b>	7.54 (7.82)	6.28 (6.60)	-2.47 (-2.88)	-3.72 (-4.08)
<b>PTCDI-CN<sub>2</sub></b>	<b>H</b>	7.99 (8.29)	6.73 (7.06)	-2.94 (-3.34)	-4.20 (-4.56)
<b>PTCDI-Cl<sub>4</sub></b>	<b>H</b>	7.74 (7.99)	6.49 (6.78)	-2.66 (-3.03)	-3.90 (-4.22)
<b>PTCDI-F<sub>2</sub></b>	<b>H</b>	7.52 (7.85)	6.20 (6.56)	-2.34 (-2.78)	-3.64 (-4.03)
<b>PTCDI-F<sub>4</sub></b>	<b>H</b>	7.63 (8.00)	6.30 (6.72)	-2.42 (-2.90)	-3.72 (-4.14)
<b>PBIF<sub>2</sub></b>	<b>CH<sub>2</sub>C<sub>3</sub>F<sub>7</sub></b>	7.59 (7.93)	6.32 (6.70)	-2.53(-2.97)	-3.78 (-4.17)
<b>PBIF<sub>4</sub></b>	<b>CH<sub>2</sub>C<sub>3</sub>F<sub>7</sub></b>	7.69 (8.07)	6.42 (6.83)	-2.61(-3.08)	-3.85 (-4.27)

<sup>a</sup> B3LYP/6-31++G\*\*/B3LYP/6-31G\*\* values are given in parentheses. <sup>b</sup> We define EA as the energy change in the process  $M + e^- \rightarrow M^-$ , where negative values indicate exothermicity upon reduction of a molecule. <sup>c</sup> IP = -(HOMO energy) and EA = LUMO energy.

The greatest effect with minimal substitution is realized by dicyano core substitution in **PTCDI-CN<sub>2</sub>**; it results in an increase in the IP value (by 0.56 eV) and more exothermic EA (by 0.66 eV). A related dicyano core-substituted compound containing fluoroalkyl groups at both ends (R<sub>3</sub> group = CH<sub>2</sub>C<sub>3</sub>F<sub>7</sub>) has been reported to exhibit air-stable high electron mobilities.<sup>5,9</sup> On the other hand, compound **20**, which constitutes one of the few reported examples of good air stability and high mobility for an *n*-channel semiconductor without strongly electron withdrawing groups,<sup>10,22</sup> shows nearly the same EA as the alkyl-substituted PTCDI **6**, whose transistor device performance quickly degrades in air (see Table 2).<sup>62</sup> This suggests that other effects such as molecular packing and film morphology might be crucial for air stability of *n*-channel organic semiconductors, as recently reported in the literature for air-stable PTCDI-based molecules with relatively high LUMO levels.<sup>19</sup>

**3.2. Electron-Vibration Coupling.** We now turn to a discussion of the intramolecular reorganization energies  $\lambda$  associated with hole and electron transfer for PTCDis: i.e., with a self-exchange reaction of the kind (for electron transfer)  $\text{PTCDI}^- + \text{PTCDI} \rightarrow \text{PTCDI} + \text{PTCDI}^-$ . Calculated values of  $\lambda$  are plotted for all the PTCDis in Figure 3. The values obtained when using a more flexible basis set with diffuse functions are collected in Table S3. As found in recent reports,<sup>61,63</sup> the  $\lambda$  estimates hardly depend on the basis set. The  $\lambda$  values are in the range of 87–245 [250–322] meV for hole [electron] transfer,  $\lambda_h$  [ $\lambda_e$ ], respectively (with the exception of PTCDis **14** and **15**; see ref 64). These values are on the same order or even smaller than those of two benchmark hole-transport materials, pentacene (95 meV)<sup>65</sup> and rubrene (159 meV),<sup>66</sup> and those of

electron-transport materials such as 1,1-diaryl-2,3,4,5-tetraphenylsiloles (490–560 meV)<sup>67</sup> and perfluoropentacene (222 meV).<sup>51</sup>

The pattern of changes in bond lengths within the perylene core upon charge transfer is nearly independent of substitution (see Figure 4). The most significant geometrical changes, on the order of 0.02 Å, take place within the C–C bonds in the bay region (bonds 7 and 8) upon oxidation and within the C–C bonds along the whole molecular periphery (bonds 4–8) upon reduction; this is in line with the HOMO and LUMO wave function patterns in unsubstituted PTCDI (see Figure 2).

Among the end- and/or core-substituted PTCDis, the net effect on electron transfer is always to increase  $\lambda_e$ , with alkyl groups giving the smallest values (on the order of 262–272 meV for **2–8**; see Figure 3). For hole transfer, it is interesting that end substitution with alkyl aromatic groups (**19–30**) lowers the reorganization energy  $\lambda_h$  significantly, for instance, by up to 65 meV in **23** (we note that normal-mode analyses indicate that this is due to variations in the contributions of a large number of vibrational modes to the reorganization energy, without any clear-cut pattern).

(64) Substitutions with phenylethoxy or azobenzene groups on the imide nitrogens strongly impact the reorganization energies for hole transfer, with values of 307 and 467 meV for PTCDis **14** and **15**, respectively. This is consistent with the observed significant geometrical relaxations on the lateral substituents upon oxidation. Note that the phenyl rings of the azobenzene moiety in PTCDI **15** are twisted around the N=N bond by about 14 and 16°, respectively, in the cation state, while they are nearly coplanar in the neutral state; in PTCDI **14**, the twist angles between the phenyl rings and the perylene plane is reduced from 76 to 51° on going from the neutral to the cation state.

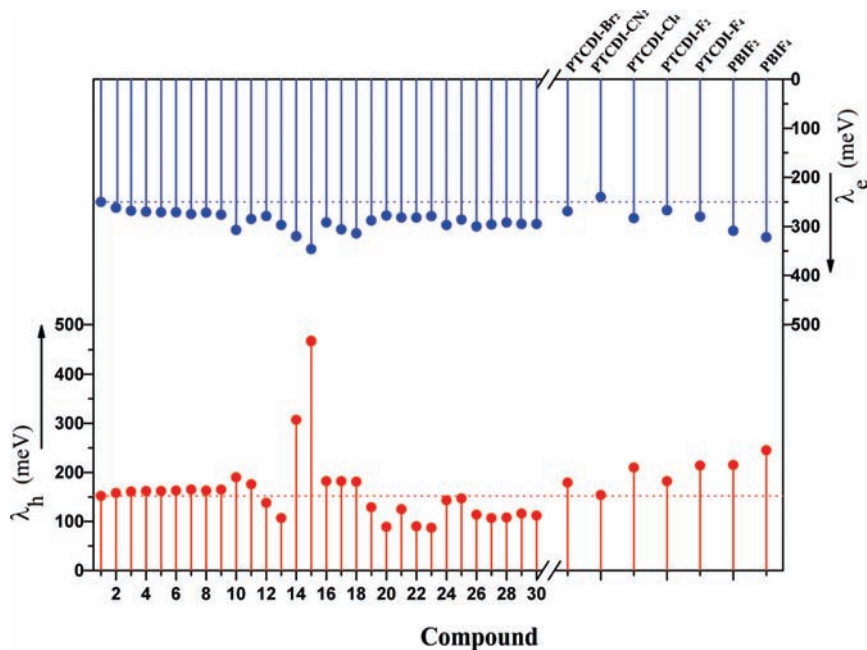
(65) Malagoli, M.; Coropceanu, V.; da Silva, D. A.; Bredas, J. L. *J. Chem. Phys.* **2004**, *120*, 7490–7496.

(66) da Silva, D. A.; Kim, E. G.; Bredas, J. L. *Adv. Mater.* **2005**, *17*, 1072.

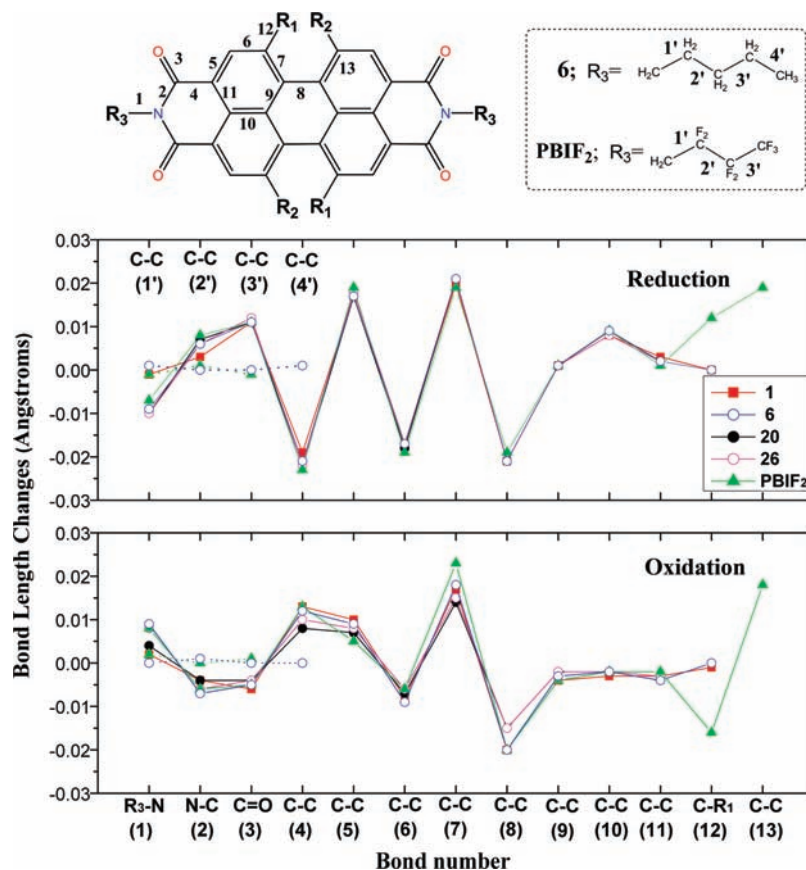
(67) Zhan, X. W.; Risko, C.; Amy, F.; Chan, C.; Zhao, W.; Barlow, S.; Kahn, A.; Bredas, J. L.; Marder, S. R. *J. Am. Chem. Soc.* **2005**, *127*, 9021–9029.

(62) Chesterfield, R. J.; McKeen, J. C.; Newman, C. R.; Frisbie, C. D.; Ewbank, P. C.; Mann, K. R.; Miller, L. L. *J. Appl. Phys.* **2004**, *95*, 6396–6405.

(63) Pan, X. M.; Cui, L. L.; Lui, L. L.; Yang, G. C.; Su, Z. M.; Wang, R. S. *Chem. Phys. Lett.* **2008**, *466*, 37–43.



**Figure 3.** Intramolecular reorganization energies for hole ( $\lambda_h$ ) and electron ( $\lambda_e$ ) transfer in all the PTCDis under study.

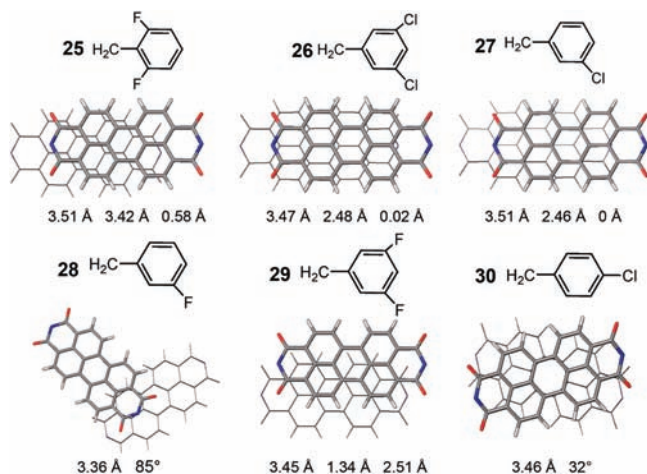


**Figure 4.** Calculated changes in bond length in isolated PTCDis **1**, **6**, **20**, **26**, and **PBIF<sub>2</sub>** upon reduction (top panel) and oxidation (bottom panel). The evolutions of the C–C bond lengths in the lateral substituents of **6** and **PBIF<sub>2</sub>** are depicted as dashed lines.

Substitution with phenylalkyl groups (where the alkyl segment has at least two carbons) on the nitrogens provides the strongest reduction in  $\lambda_h$  (**20**, **22**, and **23**), while modestly increasing  $\lambda_e$  (slightly larger than alkyls). The benzyl group is much weaker in lowering  $\lambda_h$  (with a value of 129 meV for **19**); however, halogenation of the phenyl moiety (**26**–**30**) further lowers  $\lambda_h$ ,

with the smallest values found in **27** (107 meV), while slightly increasing  $\lambda_e$ . We note, however, that the insertion of halogenated atoms (F, Cl, or Br) on the perylene core increases  $\lambda_h$ .

Upon reduction or oxidation, the core substitution redistributes the geometric relaxation mostly within the perylene core, in such a way that some bonds stretch/contract more while other bonds



**Figure 5.** Stacking patterns of two adjacent perylene moieties in end-substituted PTCDI with halogenated aromatic groups, projected down the normal to the perylene plane, based on the X-ray structures of ref 40. For each structure, the lateral substituents ( $R_3$  groups) are given. The three numbers below each diagram represent the stacking distance between neighboring molecules and the long- and short-axis displacements; for **28** and **30**, the rotation angle is given in place of displacements.

do less than in unsubstituted PTCDI (see Figure 4). Core halogenation is found to increase  $\lambda_h$  and  $\lambda_e$  (by about 30 and 20 meV, respectively, upon insertion of two halogenated atoms); this is attributed to the contributions from the significant geometric relaxations of the C–halogen bonds, which amount to  $\pm 0.015$  Å for C–F and  $\pm 0.02$  Å for C–Cl and C–Br. On the other hand, dicyano-core substitution does not affect  $\lambda_h$  and slightly lowers  $\lambda_e$  by 10 meV; the geometric relaxation involving CN following a slight charge transfer to CN ( $\pm 0.06e$ ) is minimal, resulting in no (or little) net change in  $\lambda$ .

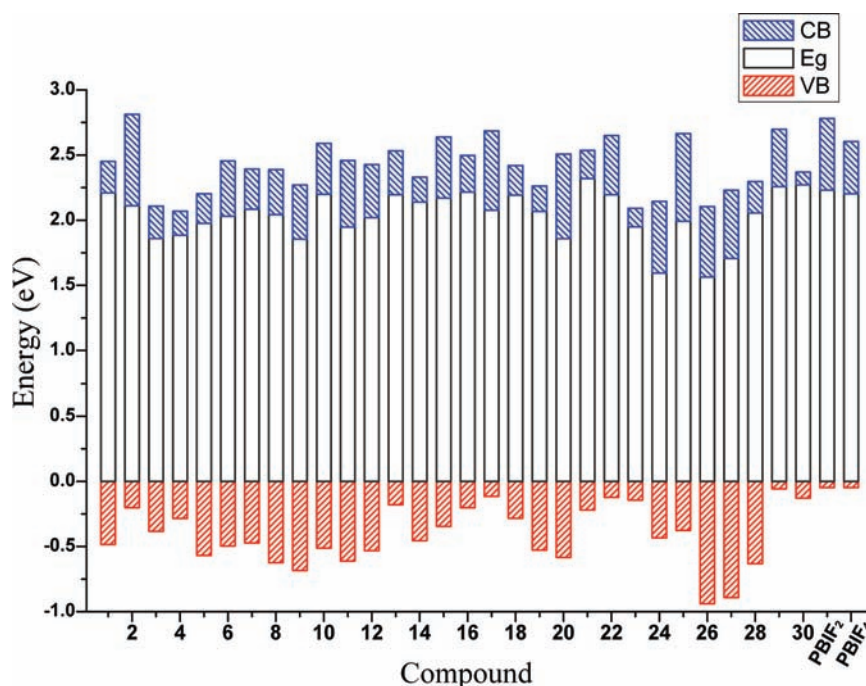
For the systems under study, it appears that additivity of the effects between the core and end substitutions also applies for  $\lambda$ . When we consider the end- and core-substituted cases, **PBIF**<sub>2</sub> and **PBIF**<sub>4</sub>, the reorganization energies can be obtained by

adding an end contribution of 30 [40] meV in  $\lambda_h$  [ $\lambda_e$ ], as incurred with the  $\text{CH}_2\text{C}_3\text{F}_7$  end group, to those of the core-substituted **PTCDI-F**<sub>2</sub> and **PTCDI-F**<sub>4</sub>, respectively.

**3.3. Intermolecular Electronic Coupling.** In the crystal, the perylene cores of the various PTCDI are arranged in stacks with molecules 3.31–3.55 Å apart (for comparison, a distance of 3.35 Å is found between sheets in graphite). In order to avoid unfavorable interactions among adjacent molecules due to substituents, relative displacements occur along the short and long molecular axes, or a rotation around the stacking axis. It is notable that small changes in the substitution pattern dramatically change the molecular packing (see Figure 5). For instance, replacing Cl with F at the meta position of the phenyl ring on going from **27** to **28** results in a rotation of the molecules around the stacking axis and transforms the color of the crystal from black-blue to dark red.<sup>40</sup>

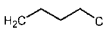
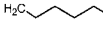
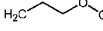
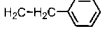

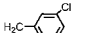

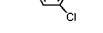
The bandgaps and conduction (CB) and valence (VB) bandwidths from the calculated band structures of all PTCDI crystals are plotted in Figure 6. The very large variation in bandwidths underlines the impact of molecular packing on transport properties. Notably, valence bandwidths close to 1 eV are obtained for the chlorobenzyl-substituted PTCDI **26** and **27**; when comparison is made among DFT results, these bandwidths are even larger than those of two prototypical high-mobility organic crystals, pentacene<sup>68,69</sup> and rubrene.<sup>66</sup> For some of the PTCDI, measured field-effect electron mobilities are available,<sup>1,3,7,10,11,22</sup> the derivatives that exhibit high electron mobilities ( $>0.1$  cm<sup>2</sup> V<sup>-1</sup> s<sup>-1</sup>), namely, **6**, **8**, **20**, and **PBIF**<sub>2</sub>, all have large calculated bandwidths (see Table 3). On the basis of the bandwidth values alone, therefore, good ambipolar charge-transport properties might be expected for **11**, **26**, and **27** (with both valence and conduction bandwidths larger than 0.5 eV), for which, to the best of our knowledge, mobility measurements have not yet been reported.

We emphasize that molecular packing, through band narrowing or widening, also impacts the transport levels to an extent that is far greater than intramolecular functionalization does.



**Figure 6.** Calculated band gaps and bandwidths of the PTCDI crystals. The zero energy is taken to correspond to the top of the valence band.

**Table 3.** Calculated Valence (VB) and Conduction (CB) Bandwidths and Band Gaps for the PTCDis with Large Bandwidths (See the Supporting Information for the Full Table)

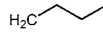
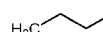


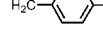


Compound	R <sub>3</sub> -Group		Band gap (meV)	VB <sup>a</sup> (meV)	CB <sup>a</sup> (meV)
1	H	[Ref. 43]	2.209	484	242
6		[Ref. 38]	2.031	497	424
8		[Ref. 47]	2.042	624	346
11		[Ref. 38]	1.947	612	511
20		[Ref. 38]	1.858	583	649
24		[Ref. 38]	1.595	433 (898) <sup>b</sup>	549
26		[Ref. 40]	1.564	939	540
27		[Ref. 40]	1.706	892	524
29		[Ref. 40]	2.258	57	440
PBIF <sub>2</sub>	CH <sub>2</sub> C <sub>3</sub> F <sub>7</sub>	[Ref. 7]	2.231	48	549

<sup>a</sup> The bandwidth is evaluated as the energy difference between the energy maximum and minimum of the topmost valence (or bottommost conduction) band. <sup>b</sup> Width of a subband that originates from the HOMO-2 levels (see text for details).

Packing induces changes in band gap by  $-0.64$  to  $+0.11$  eV with respect to unsubstituted PTCDI, while intramolecular modifications of the HOMO–LUMO gap occur only in the range  $-0.01$  to  $+0.06$  eV (except for **24** with a change of  $-0.17$  eV) (see Figure 6 and Figure S1 in the Supporting Information).

To better understand the large bandwidth variations in the PTCDis from the perspective of molecular packing, we discuss

**Table 4.** Calculated Transfer Integrals (in meV) for the HOMO ( $t_H$ ) and LUMO ( $t_L$ ) Levels in Cofacial Dimers Extracted from the Experimental Crystal Structures of the PTCDis<sup>a</sup>

Compound	R <sub>3</sub> -Group	d <sup>a</sup>	d <sub>long</sub> <sup>a</sup>	d <sub>short</sub> <sup>a</sup>	t <sub>H</sub> <sup>b</sup>	t <sub>L</sub> <sup>b</sup>
6		3.37	3.10	1.30	-104 (-108)	-41 (-38)
11		3.47	3.13	0.68	-120 (-115)	98 (98)
20		3.48	3.20	0.39	-117 (-124)	141 (145)
24		3.47	2.67	0.36	-87, -189 <sup>c</sup> (-195)	114 (113)
26		3.47	2.48	0.02	-192 (-208)	119 (122)
27		3.51	2.46	0	-179 (-194)	116 (114)
29		3.45	1.34	2.51	-18	-95
PBIF <sub>2</sub>	CH <sub>2</sub> C <sub>3</sub> F <sub>7</sub>	3.30	1.25	3.93	2	107

<sup>a</sup>  $d$  is the intermolecular distance, and  $d_{long}$  and  $d_{short}$  are the displacements along the long and short molecular axes, respectively. Values are given in angstroms (Å). <sup>b</sup> Values in parentheses are calculated for a pair of unsubstituted PTCDI molecules placed in the same corresponding spatial arrangement. <sup>c</sup> Calculated for the monomer HOMO-2 levels.

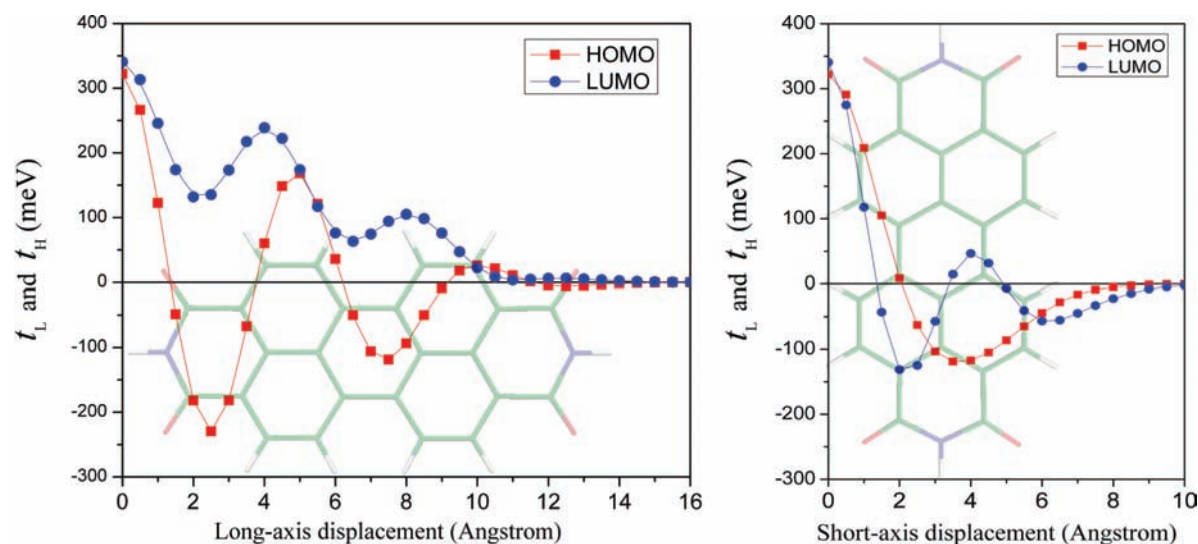
below in greater detail their band structures, in conjunction with a pairwise breakdown of intermolecular electronic coupling.

Values of the transfer integral for cofacial dimers in the PTCDI crystals are collected in Table 4. We recall that in the context of a one-dimensional tight-binding model, the bandwidth  $W$  can be calculated from the transfer integral  $t$  using  $W = 4t$ . Comparison of the bandwidths estimated in this way with those obtained directly from the band structure (for **26**, for instance,  $4t_H [4t_L] = 768 [476]$  meV and the valence [conduction] bandwidth is 939 [540] meV) indicates that, in most instances, interactions in a cofacial dimer configuration (and thus a one-dimensional  $\pi$  stack) indeed account for much of the intermolecular electronic coupling in the PTCDI crystals. In the particular case of **6**, where  $4t_L (=164$  meV) is only 40% of the actual bandwidth (see Table 4), a large displacement of 1.3 Å along the short molecular axis reduces intrastack dimer interactions to 41 meV but instead promotes new *interstack* dimer interactions (40 meV); together they lead to a strong dispersion in the conduction band.

It is not surprising to find in Table 4 that the transfer integrals for dimers extracted directly from the crystal structures nearly coincide with those for the unsubstituted PTCDI dimers placed in the corresponding spatial arrangements. As we discussed earlier, the end substituents make insignificant contributions to the HOMO and LUMO wave functions of the substituted PTCDis. What this allows us to do is to investigate in a simple way the impact of long-axis and short-axis displacements on the electronic coupling; we do so by sliding one molecule over the other in a cofacial configuration, without having to consider the substituents explicitly. The results are shown in Figure 7.

The alternating bonding–antibonding pattern of the HOMO along the long molecular axis leads to multiple sign changes for  $t_H$  in the course of a long-axis translation (see Figure 7). On the other hand,  $t_L$  decreases without changing sign because the





**Figure 7.** Evolution of the HOMO and LUMO transfer integrals for an unsubstituted PTCDI cofacial dimer, as a function of the long-axis (left) and short-axis (right) displacements of the top molecule. The intermolecular distance is set at 3.40 Å, the average intermolecular separation found in the PTCDI crystals along the  $\pi$ -stacks.

LUMO bonding–antibonding pattern does not change phase along the long molecular axis (see Figure 2 for the wave function patterns). The HOMO and LUMO electronic couplings remain significant for long-axis displacements of 2.40–3.20 Å, which are those found among the systems that present small offsets along the short axis; in these compounds,  $t_H$  [ $t_L$ ] values range between –220 and –136 [134 and 191] meV (see Table 4). The much steeper evolution of  $t_H$  vs long-axis displacement is expected to make crystal vibrations (phonons) involving long-axis librations impact more strongly hole transport than electron transport (leading to a greater nonlocal electron–phonon coupling for holes).

The intermolecular electronic coupling dies out rapidly in the course of short-axis translation (see Figure 7), which is mainly due to the alternating HOMO/LUMO phase and the small spatial dimension of the molecule along the short molecular axis. For the PTCDI crystals with dominant one-dimensional character such as **11**, **20**, **24**, **26**, and **27**, the short-axis displacements are found to remain well within 1 Å, up to which the electronic coupling remains strong ( $t_H > 200$  meV and  $t_L > 110$  meV). We can also expect short-axis librations in the crystal to strongly impact both hole and electron transport.

Below we examine the band structure more closely for a subset of the PTCDI listed in Table 4. In general, the valence [conduction] band consists of subbands arising from the interactions among the monomer HOMO [LUMO] levels. For nondegenerate monomer energy levels, the number of these subbands is equal to the number of molecules in the *primitive* unit cell, and many of the PTCDI that we are studying have one molecule per cell. In the particular case of **20**, whose band structure is shown in Figure 8a, the primitive unit cell contains two translationally inequivalent molecules, which gives rise to two subbands. Because the inequivalent molecules interact with each other only very weakly, the subbands appear nearly degenerate in both the valence and conduction bands.

In general, strongly dispersive bands are seen only in certain regions of the first Brillouin zone; the appearance of both

dispersive and flat bands is a reflection of anisotropy in the charge-transport properties of the crystal. We recall that **20** presents well-defined one-dimensional  $\pi$ -stacks, which translates into strongly dispersive bands in the  $\Gamma A$  and  $\Gamma V$  directions. The flat band in the  $VY$  and  $MU$  directions (which correspond to the  $c$  direction in direct space) is a clear indication of the weak interstack interactions (that we discussed above as a source of band degeneracy in **20**).

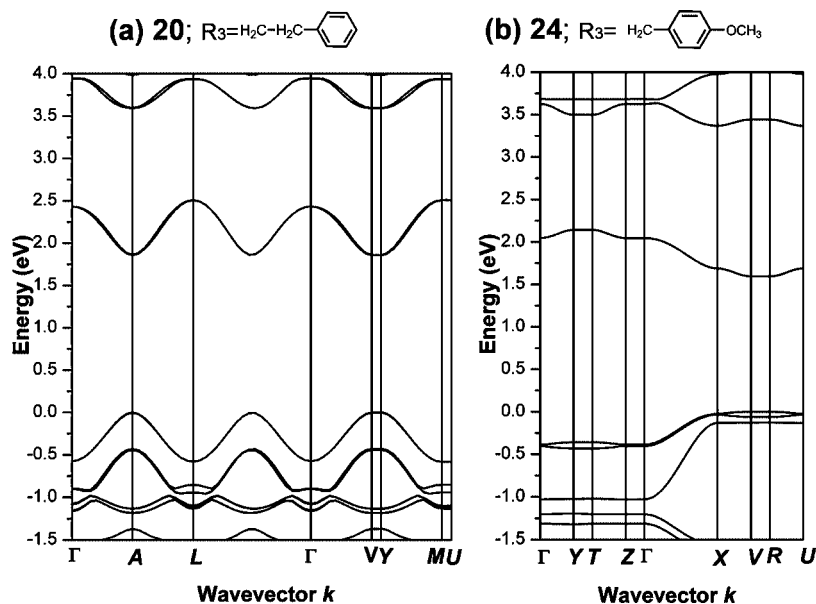
As noted earlier in the discussion of the single-molecule transport levels, **24** differentiates itself from the rest of the PTCDI in terms of its HOMO level; the HOMO is not found on the perylene core but is localized on the methoxyphenyl part of the end substituents and is (nearly) doubly degenerate (see Figure 2). As a result, the top valence band of its crystal, shown in Figure 8b, arises from interactions among the  $\pi$ -stacked substituents, not the perylene cores. Comparison of the transfer integrals for the degenerate HOMO and HOMO-1 levels of the monomer ( $4t_H = 4t_{H-1} = -348$  meV) with the dispersion of the top two nearly degenerate valence subbands ( $W = 433$  meV) confirms the main one-dimensional character of the interactions among the substituents. The HOMO-2 levels (corresponding to the HOMO of the other PTCDI), separated from the upper levels by only 0.16 eV, form the third subband just below the top valence band; its band dispersion ( $W = 898$  meV) is accounted for mostly by the pairwise cofacial interactions of the HOMO-2 levels ( $4t = -756$  meV).

We have shown that chemical substitution affects the bulk transport levels and the intermolecular electronic coupling of the PTCDI, not by changing the electronic structure at the single-molecule level but by changing the molecular packing. The case of **24** may actually provide an intriguing additional handle to the engineering transport properties of PTCDI. Namely, by further aligning the substituent HOMO level to match exactly the perylene core HOMO level, one could incorporate two independent transport channels, one via stacked substituents and the other via stacked perylene cores; this could be achieved by substitution of the phenyl group with  $\pi$ -electron donors weaker than the methoxy group in **24**.

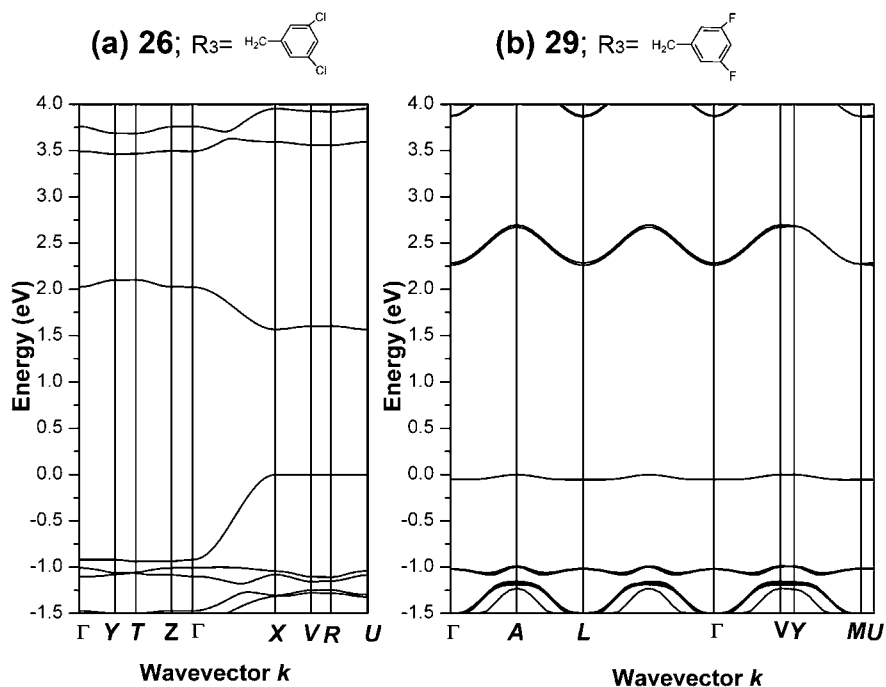
The impact of molecular packing on transport parameters and transport level can be best illustrated by comparing **26** with **29**.

(68) de Wijs, G. A.; Mattheus, C. C.; de Groot, R. A.; Palstra, T. T. M. *Synth. Met.* **2003**, *139*, 109–114.

(69) Hummer, K.; Ambrosch-Draxl, C. *Phys. Rev. B* **2005**, *72*, 205205.



**Figure 8.** Band structures of two phenylalkyl-substituted PTCDI crystals: (a) **20** ( $C2/c$  space group,  $a = 20.13$  Å,  $b = 4.74$  Å,  $c = 29.95$  Å, and  $\beta = 103.35^\circ$ ) and (b) **24** ( $P1$  space group,  $a = 4.39$  Å,  $b = 9.71$  Å,  $c = 17.11$  Å,  $\alpha = 98.82^\circ$ ,  $\beta = 91.07^\circ$ , and  $\gamma = 101.58^\circ$ ). The energies are plotted along directions in the first Brillouin zone connecting the points:  $\Gamma = (0,0,0)$ ,  $A = (0.5,0,0)$ ,  $L = (0.5,0.5,0)$ ,  $V = (0,0.5,0)$ ,  $Y = (0,0.5,0.5)$ ,  $M = (0.5,0.5,0.5)$  and  $U = (0.5,0.5,0)$  for the band structure of **20**;  $\Gamma = (0,0,0)$ ,  $Y = (0,0.5,0)$ ,  $T = (0,0.5,0.5)$ ,  $Z = (0,0,0.5)$ ,  $X = (0.5,0,0)$ ,  $V = (0.5,0.5,0)$ ,  $R = (0.5,0.5,0.5)$ , and  $U = (0.5,0,0.5)$ , for the band structure of **24**. The zero of the energy scale is set as the top of the valence band.



**Figure 9.** Electronic band structures of two PTCDI crystals: (a) **26** ( $P1$  space group,  $a = 4.26$  Å,  $b = 10.09$  Å,  $c = 17.35$  Å,  $\alpha = 103.84^\circ$ ,  $\beta = 92.42^\circ$ , and  $\gamma = 100.19^\circ$ ) and (b) **29** ( $C2/c$  space group,  $a = 20.68$  Å,  $b = 4.47$  Å,  $c = 22.10$  Å, and  $\beta = 103.12^\circ$ ). The energies are plotted along directions in the first Brillouin zone connecting the points:  $\Gamma = (0,0,0)$ ,  $Y = (0,0.5,0)$ ,  $T = (0,0.5,0.5)$ ,  $Z = (0,0,0.5)$ ,  $X = (0.5,0,0)$ ,  $V = (0.5,0.5,0)$ ,  $R = (0.5,0.5,0.5)$ , and  $U = (0.5,0,0.5)$ , for the band structure of **26**;  $\Gamma = (0,0,0)$ ,  $A = (0.5,0,0)$ ,  $L = (0.5,0.5,0)$ ,  $V = (0,0.5,0)$ ,  $Y = (0,0.5,0.5)$ ,  $M = (0.5,0.5,0.5)$ , and  $U = (0.5,0.5,0)$  for the band structure of **29**. The zero of the energy scale is set as the top of the valence band.

As in the case of **27** vs **28** that we discussed earlier, there exists a notable difference of crystal color between these two compounds (black-blue for **26** and dark red for **29**) due to a difference in molecular packing, a difference caused by a seemingly modest difference in functionalization (Cl vs F) of the end substituent (see Figure 5). When their band structures are compared (see Figure 9), a dramatic reduction in the valence bandwidth is found for **29** (57 meV for **29** vs 939 meV for **26**),

while the conduction bandwidth is substantial for both (440 meV for **29** vs. 540 meV for **26**). The strong conduction band dispersion occurs in the  $\Gamma X$  subzone for **26** and in  $\Gamma A$  and  $\Gamma V$  for **29** (corresponding approximately to the respective  $\pi$ -stacking directions of the perylene cores). Again, intermolecular electronic coupling in the crystal is very well represented by the cofacial pairwise interactions for both **26** and **29**, as seen also in comparison to the transfer integral calculations (see Table 4).

The fact that **29** has a larger short-axis dimer displacement of 2.51 Å but a smaller long-axis displacement of 1.34 Å than **26** reiterates the importance of the actual wave function overlap, and not the area overlap, in the determination of the electronic coupling.<sup>70</sup> Note that the long-axis displacement of 1.34 Å in **29** corresponds to a vanishing HOMO transfer integral in the plot of Figure 7, which contributes to the small width of the valence band. It is also of interest to mention that the substantial valence and conduction bandwidths in **26** result in a marked reduction of the band gap, which is calculated to be 0.7 eV lower than in **29** (see also Figure 6).

**3.4. Implications for Band or Hopping Transport.** We now turn to a discussion of what our estimates for the charge-transport parameters in PTCDI crystals could imply in the framework of the two limiting transport regimes: namely, the band and hopping regimes.

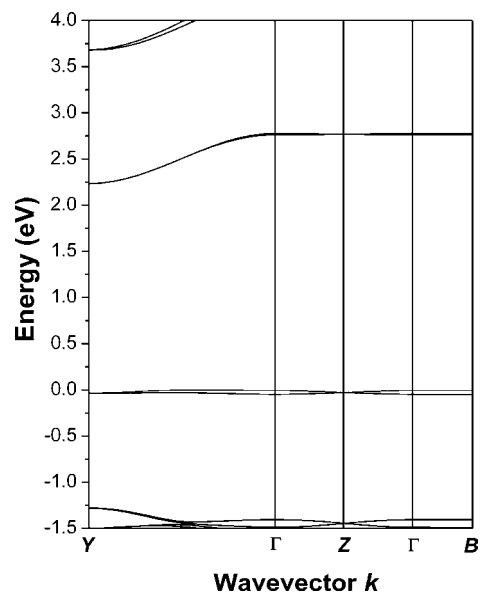
When electronic coupling prevails over electron–vibration (phonon) coupling (i.e., when the energy gained via charge delocalization is larger than that gained via charge localization and polaron formation),<sup>34</sup> a band regime can manifest at low temperatures in perfectly ordered systems. In the case of wide bands where excess electrons [holes] occupy states near the bottom [top] of the conduction [valence] band, the charge carrier mobility is directly related to the carrier effective mass. The effective mass for electrons [holes] can be computed from the band structures at the conduction [valence] band extremum (which provides for the thermally populated levels). The effective mass can be viewed as the mass of the elementary charge carrier as modified by the potential of the crystal environment.<sup>71</sup> Within the PTCDI series, compound **26** presents the widest bands (see Table 3). The smallest hole effective mass in **26** is found along (approximately) the stacking direction; it amounts to  $0.84m_0$  (where  $m_0$  denotes the free electron mass at rest), which is smaller than the effective mass reported experimentally for rubrene ( $1 < m/m_0 < 1.3$ ).<sup>72</sup> The smallest electron effective mass, also found along the  $\pi$ -stacking direction, is  $1.4m_0$ . Interestingly, the electron effective mass in **PBIF**<sub>2</sub>, for which a high mobility on the order of  $0.35 \text{ cm}^2/\text{Vs}$  has been reported experimentally,<sup>7</sup> is calculated to be  $1.78m_0$  along the stacking direction; the band structure of **PBIF**<sub>2</sub> is shown in Figure 10.

According to the band theory, the carrier mobility in wide bands is given by<sup>71</sup>

$$\mu = \frac{q\tau}{m} \quad (1)$$

where  $q$  is the carrier charge,  $\tau$  is the mean free time between scattering events (or mean relaxation time of the band state), and  $m$  is the effective mass of the charge carrier. In the isotropic relaxation time approximation, the mobility and its orientational anisotropy are dictated by the effective mass. In this context, if we assume similar  $\tau$  values in the three systems, **26** can be expected to have higher electron mobility than **PBIF**<sub>2</sub> and higher hole mobility than rubrene.

When electron–phonon coupling becomes comparable or stronger than electronic coupling, charge localization takes place and transport is expected to occur via a charge-hopping



**Figure 10.** Electronic band structure of the **PBIF**<sub>2</sub> crystal ( $P2_1/c$  space group,  $a = 17.46 \text{ \AA}$ ,  $b = 5.28 \text{ \AA}$ ,  $c = 15.28 \text{ \AA}$ , and  $\beta = 110.90^\circ$ ). The energies are plotted along directions in the first Brillouin zone connecting the points:  $Y = (0,0,5,0)$ ,  $\Gamma = (0,0,0)$ ,  $Z = (0,0,5)$ , and  $B = (0.5,0,0)$ . The zero of the energy scale is set as the top of the valence band.

mechanism; in this case, the carrier hops can be described as a self-exchange electron-transfer process between a charged molecule and an adjacent neutral molecule.<sup>34</sup> The electron transfer or hopping rate can be estimated in the context of semiclassical Marcus theory as<sup>73</sup>

$$k_{\text{ET}} = t^2 \sqrt{\frac{\pi}{\hbar^2 k_B T \lambda}} \exp\left(-\frac{\lambda}{4k_B T}\right) \quad (2)$$

where  $\lambda$  is the overall reorganization energy,  $t$  is the transfer integral,  $k_B$  is the Boltzmann constant,  $T$  is the temperature, and  $\hbar$  is the Planck constant divided by  $2\pi$ .

At high temperature, the mobility can be approximated as<sup>74</sup>

$$\mu = \frac{qd^2}{k_B T} k_{\text{ET}} \quad (3)$$

where  $d$  is the intermolecular distance between adjacent molecules (which defines the length of the carrier hops).

By injecting into eqs 2 and 3 the calculated charge-transport parameters for the PTCDI materials that display promising hole and/or electron transport characteristics (i.e., large electronic couplings together with small reorganization energies), rough estimates of the transfer rates and thus carrier mobilities can be made (see Table 5). Then, by comparing the transport parameters calculated for PTCDI materials that have not been experimentally investigated yet to those that have been reported, we are in a position to identify compounds that would warrant experimental investigations.

We recall that only the intramolecular contributions to the reorganization energies have been considered here, as the nuclear polarization contributions are expected to be significantly smaller.<sup>75</sup> In spite of all the approximations made, the electron mobilities in **6**, **20**, and **PBIF**<sub>2</sub> are calculated to be in good agreement with currently available experimental values (Table 5).<sup>1,7,10,22</sup> Interestingly, similar electron transfer rates ( $\sim 2 \times 10^{13} \text{ s}^{-1}$ ) and mobilities ( $\sim 0.5 \text{ cm}^2 \text{ V}^{-1} \text{ s}^{-1}$ ) are predicted for

(70) Bredas, J. L.; Calbert, J. P.; da Silva, D. A.; Cornil, J. *Proc. Natl. Acad. Sci. U.S.A.* **2002**, *99*, 5804–5809.

(71) Seeger, K. *Semiconductor Physics: An Introduction*, 9th ed.; Springer-Verlag: Berlin, 2004.

(72) Li, Z. Q.; Podzorov, V.; Sai, N.; Martin, M. C.; Gershenson, M. E.; Di Ventra, M.; Basov, D. N. *Phys. Rev. Lett.* **2007**, *99*, 016403.

**Table 5.** Calculated Transfer Rates ( $k_{ET}$ ) and Mobilities ( $\mu$ ) for the End- and Core-/End-Substituted PTCDI Molecules, with Experimental Electron Mobilities ( $\mu_{exp}$ ) Given for Comparison Where Available

Compound	R <sub>3</sub> -Group	Holes <sup>a</sup>		Electrons		
		$k_{ET}[s^{-1}]$	$\mu[cm^2V^{-1}s^{-1}]$	$k_{ET}[s^{-1}]$	$\mu[cm^2V^{-1}s^{-1}]$	$\mu_{exp}[cm^2V^{-1}s^{-1}]$
6		$9.3 \times 10^{13}$	2.1	$3.9 \times 10^{12}$	0.1	$0.10^{[Ref.11]}$
11		$1.1 \times 10^{14}$	2.4	$1.9 \times 10^{13}$	0.4	
20		$3.3 \times 10^{14}$	7.3	$4.3 \times 10^{13}$	1.0	$0.1^b [Ref. 22], 1.4^c [Ref. 10]$
24				$2.3 \times 10^{13}$	0.5	
26		$6.1 \times 10^{14}$	14	$2.4 \times 10^{13}$	0.5	
27		$5.9 \times 10^{14}$	13	$2.4 \times 10^{13}$	0.5	
29				$1.6 \times 10^{13}$	0.4	
PBIF <sub>2</sub>	CH <sub>2</sub> C <sub>3</sub> F <sub>7</sub>			$1.7 \times 10^{13}$	0.4	$0.35^{[Ref. 7]}$

<sup>a</sup> As PTCDis have been primarily considered as n-channel materials, experimental measurements of hole mobilities have been lacking. <sup>b</sup> In a vacuum-deposited organic thin-film transistor. <sup>c</sup> In a single-crystalline microwire transistor.

systems **11**, **24**, **26**, **27**, and **29**, for which (to the best of our knowledge) no experimental measurements are available. For hole transfer, the mobility at room temperature in PTCDis **6**, **11**, **20**, **26**, and **27** should be even larger than electron mobilities, with calculated values  $\sim 14 \text{ cm}^2 \text{ V}^{-1} \text{ s}^{-1}$  for **26**; for comparison, an estimate of hole mobility around  $8 \text{ cm}^2 \text{ V}^{-1} \text{ s}^{-1}$  is predicted for rubrene when using the transport parameters calculated at the same theoretical level ( $t = 83 \text{ meV}$ ,  $\lambda = 159 \text{ meV}$ ).<sup>66</sup>

Thus, in the context of the hopping regime, we find the following.

(i) PTCDis **11**, **26**, and **27** appear to be promising both as *n*-channel and *p*-channel semiconductors, with hole mobilities predicted to be up to 1 order of magnitude larger than electron mobilities, primarily because of the larger internal reorganization energies for electrons than for holes.

(ii) Large intrinsic hole mobilities are predicted for **20** and **PBIF<sub>2</sub>**, which are already known as good *n*-channel materials.

(iii) The intrinsic electron mobilities in **24** and **29** might even be somewhat larger than that measured for **PBIF<sub>2</sub>**, with values on the order of  $0.5 \text{ cm}^2 \text{ V}^{-1} \text{ s}^{-1}$ .

#### 4. Conclusions

We have explored at the DFT level the impact of functionalization on the charge-transport parameters of 37 PTCDI crystals, with a focus on end and core substitutions. Our results indicate that substitution can vary the energies of the molecular levels by 0.01 to 0.06 eV with end and core substitutions providing nearly additive effects. The intramolecular reorganization energy for electrons is found to increase upon both end and core substitutions. On the other hand, a decrease in reorganization energy for holes is found upon alkylphenyl end substitution, while the insertion of halogenated atoms on the perylene core results in larger values.

Depending on the nature and positions of the substituents, the solid-state packing and resulting electronic and charge-transport properties are found to be strongly modified; for instance, the bandwidths are tuned over a range of about

0.05–0.94 eV and changes in band gap are in the range of  $-0.64$  to  $+0.11$  eV. The strongest band dispersions in the crystal are found essentially along the one-dimensional (1D)  $\pi$ -stacking direction; short-axis displacements have to be kept to a minimum to give rise to large electronic couplings. Wide hole and electron transport bands (and low effective masses for both holes and electrons) are found in end-substituted PTCDis with chlorinated aromatic groups.

The intrinsic electron mobilities calculated on the basis of the semiclassical Marcus theory are found to be in good agreement with available experimental data. These results allow us to identify PTCDI crystals with promising hole and/or electron transport characteristics that warrant experimental investigations.

The tunability of electronic coupling and transport levels via molecular packing available in the PTCDI family is related to the large, planar shape of the molecular backbone, which provides the possibility of greatly varying the intermolecular wave function overlap. Although the prediction of crystal packing currently remains beyond reach, our study clearly demonstrates that a remarkably large range of transport properties can be achieved via crystal engineering of existing molecular backbones. Thus, screening of molecules in structural databases using quantum-chemical tools can not only advance our understanding of structure-transport-property relationships but also help uncover known materials for new applications.

**Acknowledgment.** We thank Professor C.D. Frisbie at the University of Minnesota and Dr. Veaceslav Coropceanu at Georgia Tech for stimulating discussions. This work has been primarily supported by the MRSEC Program of the National Science Foundation under Award Number DMR-0819885. M.C.R.D. acknowledges the Spanish Ministry of Education and Science (MEC)

(73) Marcus, R. A. *Rev. Mod. Phys.* **1993**, *65*, 599–610.

(74) Pope, M.; Swenberg, C. E. *Electronic Processes in Organic Crystals and Polymers*, 2nd ed.; Oxford University Press: New York, 1999.

(75) Norton, J. E.; Bredas, J. L. *J. Am. Chem. Soc.* **2008**, *130*, 12377–12384.

for an MEC/Fulbright Postdoctoral Fellowship at Georgia Tech. We are grateful to the Minnesota Supercomputing Institute for use of their computational facilities.

**Supporting Information Available:** Text giving details of the Monkhorst–Pack  $k$ -point mesh used for the PTCDI crystals; Table S1, giving crystallographic parameters for the unit cells of all the PTCDI crystals; Table S2, giving ionization potentials and electron affinities of all the PTCDI systems, obtained from  $\Delta$ SCF and KT calculations at the B3LYP/6-31G\*\* level; Figure S1, giving B3LYP/6-31G\*\* estimates of the HOMO–LUMO

gap ( $E_g$ ) for the isolated PTCDI molecules; Table S3, giving intramolecular reorganization energies for hole ( $\lambda_h$ ) and electron ( $\lambda_e$ ) transfer in all the PTCDI systems; Table S4, giving adiabatic potential (AP) surfaces and normal mode (NM) estimates of the intramolecular reorganization energies at the B3LYP/6-31G\*\* level; tables giving Cartesian coordinates and energies of all calculated structures; and complete ref 31. This material is available free of charge via the Internet at <http://pubs.acs.org>.

JA908173X